SCIENCE CHINA
Chemistry

•ARTICLES•
SPECIAL ISSUE: 2020 Emerging Investigator Issue

October 2020 Vol.63 No.10: 1449–1460
https://doi.org/10.1007/s11426-020-9785-7

High-performance all-polymer solar cells with only 0.47 eV energy loss

Qiang Wu[1†], Wei Wang[1†], Tao Wang[1], Rui Sun[1], Jing Guo[1], Yao Wu[1], Xuechen Jiao[4], Christoph J. Brabec[5], Yongfang Li[2] & Jie Min[1,2,3*]

[1]*The Institute for Advanced Studies, Wuhan University, Wuhan 430072, China;*
[2]*Beijing National Laboratory for Molecular Sciences, Beijing 100190, China;*
[3]*Key Laboratory of Materials Processing and Mold (Ministry of Education), Zhengzhou University, Zhengzhou 450002, China;*
[4]*Department of Materials Science and Engineering, Monash University; Australian Synchrotron, Clayton, Victoria, Australia;*
[5]*Institute of Materials for Electronics and Energy Technology (i-MEET), Friedrich-Alexander-Universität-Erlangen-Nürnberg, Erlangen, Germany*

Received June 1, 2020; accepted June 3, 2020; published online July 2, 2020

The field of all-polymer solar cells (all-PSCs) has experienced rapid development during the past few years, mainly driven by the development of efficient polymer acceptors. However, the power conversion efficiencies (PCEs) of the all-PSCs are still limited by insufficient light absorption of the donor/acceptor blend and large energy loss in devices. We herein designed a polymer acceptor PYT1 constructed n-type molecular acceptor Y5-C20 as the key building block and blended it with a polymer donor PM6 to obtain an all-polymer photoactive layer. The optimized PM6:PYT1 all-PSCs achieved a record higher PCE of 13.43% with a very low energy loss of 0.47 eV and a photoresponse of up to 900 nm compared with the Y5-C20 based device with a best PCE of 9.42%. Furthermore, the PCEs of the PM6:PYT1 all-PSCs are relatively insensitive to the 1-chloronaphthalene (CN) additive contents and active layer thickness. Our results also highlight the effect of CN additive on PM6:PYT1 morphology, *i.e.*, charge generation, and transport find an optimized balance, and radiative and non-radiative loss is simultaneously reduced in the blend. This work promotes the development of high-performance polymer acceptors and heralds a brighter future of all-PSCs for commercial applications.

all-polymer solar cells, polymer acceptor, absorption coefficient, energy loss, mechanical stability

Citation: Wu Q, Wang W, Wang T, Sun R, Guo J, Wu Y, Jiao X, Brabec CJ, Li Y, Min J. High-performance all-polymer solar cells with only 0.47 eV energy loss. *Sci China Chem*, 2020, 63: 1449–1460, https://doi.org/10.1007/s11426-020-9785-7

1 Introduction

Solution-processed polymer solar cells (PSCs) have emerged as a promising approach for solar energy harvesting due to their prominent advantages of low cost, lightweight, and flexibility [1–3]. Intense research efforts over the past years have provided a deeper understanding of the processes governing bulk heterojunction (BHJ) based PSCs design and operation, now enabling fullerene-free PSCs with power conversion efficiencies (PCEs) beyond 16% [4–6]. In general, both small molecule and polymer non-fullerene acceptors (NFAs) possess advantages such as synthetic flexibility, good solution processability, tunable energy levels, strong light absorbing properties/capabilities, and frequently good thermal and photo stresses [7–11]. Compared to the small molecular acceptors (SMAs)-based photovoltaic systems, all-polymer solar cells (all-PSCs) consisting of polymers as both donor (D) and acceptor (A) semiconductors are uniquely attractive due to their estimated broad absorp-

†These authors contributed equally to this work.
*Corresponding author (email: min.jie@whu.edu.cn)

tion bands, long-term thermal and mechanical stability, and amenability for large-scale manufacturing [11–15]. Many n-type conjugated polymers have been developed based on naphthalene diimide (NDI) [16–19], perylene diimide (PDI) [20–22], B←N-bridged bipyridine moieties [13,23], dicyanobenzothiadiazole moieties [14,24–26], and their derivatives [2,12,14,27–29]. However, the PCEs (approximately 11%) of state-of-the-art all-PSCs have lagged significantly in performance behind their SMAs counterparts, primarily due to the lack of high-performance n-type polymers with narrow-bandgaps and high absorption coefficients [2,7,27]. So far, very few polymer acceptors can yield PCEs of over 10% in all-PSCs reported in literatures (Table S1, Supporting Information online) and more importantly, all these structures are based exclusively on two kinds of electron-deficient units (Figure S1, Supporting Information online): (1) NDI-based imide embedded blocks [12] and (2) a dicyanoethylene-containing moiety, namely, IDIC [14,25,29]. Despite the great successes of the NDI-based polymer acceptors reported, such as poly[[*N*,*N*′-bis(2-octyl dodecyl)-naphthalene-1,4,5,8-bis(dicarboximide)-2,6-diyl-alt]-5,5′-(2,2′-bithiophene)] (N2200), their backbones are twisted due to their conjugated π-cores and the extruding carbonyl groups, which lowers absorption coefficient in films (*ε*, a *ε* of 3.48×10^4 cm^{-1} at 700 nm), enlarges optical bandgap (E_g^{opt}, a E_g^{opt} of 1.47 eV), restrains charge carrier transport properties, thus limiting the short-circuit current density (J_{SC}) and efficiency improvement [7,17,24]. In addition, the relatively poor miscibility in N2200-derivative-based BHJ blends is the long-standing bottlenecks, which has suffered significantly degrees of phase separation, promoting blend charge carrier recombination, and also reducing the J_{SC}, fill factor (FF) and ultimately the PCEs of such devices [19,26,30]. Another representative IDIC-based polymer acceptor is PZ1 [26], which was synthesized by embedding an A-D-A building block into the polymer backbone. Benefiting from its high absorption coefficient (1.30×10^5 cm^{-1} at 700 nm) and matching energy levels with a fluorinated wide-bandgap p-type conjugated polymer PM6 (poly[(2,6-(4,8-bis(5-(2-ethylhexyl-3-fluoro)thiophen-2-yl)-benzo[1,2-*b*:4,5-*b*′]dithiophene))-alt-(5,5-(1′,3′-di-2-thienyl-5′,7′-bis(2-ethylhexyl)benzo[1′,2′-*c*:4′,5′-c′]dithiophene-4,8-dione)]) [31], the corresponding devices achieved an optimal PCE of 11.2% with a high open-circuit voltage (V_{OC}) of 0.96 V, a J_{SC} of 17.1 mA cm^{-2} [25]. However, the medium optical bandgap (a E_g^{opt} of 1.55 eV) of PZ1 as well as its similar derivatives was an important issue that significantly limited its J_{SC} [14,26]. Regardless of that, it is still a promising strategy to introduce the popular fused-ring electron acceptor (FREA) segment into polymer backbone as a building block to design high-performance polymer acceptors.

Based on this view, developing new polymer acceptors with narrower bandgap and the increased absorption coefficient is imminent for further improving photovoltaic performance of all-PSCs, which mainly relies on the invention of new electron-deficient building blocks, especially for FREA moieties. Among various FREA-based SMAs, a family of small molecule acceptors based on the ladder-type D-A-D fused structures as central cores exhibit many advantages (such as narrow optical bandgap, deep highest occupied molecular orbital (HOMO) levels, high mobility and electron affinity, and good molecular geometry) [4,6,32,33], and greatly accelerate the development of SMA-based PSCs, achieving record-high efficiency of over 16% for single-junction PSCs [4–6,34]. Obviously, further advancement of all-PSCs requires a judicious design strategy to introduce such FREA segments into polymer acceptors that possess these essential properties.

Bearing in mind that the promising advantages of the ladder-type DAD fused cores [4,6,33,35], herein we designed and synthesized a polymer acceptor (designated as PYT1, as displayed in Figure 1(a)) constructed n-type DAD-based organic semiconductor Y5-C20 (2,2′-((2*Z*,2′*Z*)-((12,13-bis(2-octyl dodecyl)-3,9-diundecyl-12,13-dihydro[1,2,5]thiadiazolo [3,4e]thieno[2″,3″:4′,5′]thieno[2′,3′:4,5]pyrrolo[3,2-*g*]thieno[2′,3′:4,5]thieno[3,2-*b*]-indole-2,10-diyl)bis(methanylylidene))bis(3-oxo-2,3-dihydro-1*H*-indene-2,1-diylidene)) dimalononitrile) as the key building block and thiophene as the linking units. Of note is that the designed and synthesized Y5-C20 (Scheme S1, Supporting Information online) possesses the same molecular backbone as that of Y5 but with longer alkyl side chains for improving the solubility of the resulting polymer. The embedding of Y5-C20 as the key building block is expected to preserve the merits of SMAs as mentioned above [4,14,26,32] and also to show conjugated polymers' advantages of combining the merits of tunable photophysical properties, good environmental and mechanical stresses [12,14,26]. By blending the PYT1 acceptor with the polymer donor PM6 [31], an all-PSC device with a broad absorption band that ranges from 300 to 900 nm was fabricated. Under the illumination of AM 1.5 G (100 mW cm^{-2}), the all-PSC device gives a PCE of 13.43% with a high J_{SC} of 21.50 mA cm^{-2}, which is among the top values of all-PSCs. Moreover, as compared to the Y5-C20-based system, this PYT1-based all-polymer system possesses good mechanical stability, and relative insensitivity to CN additive contents and active layer thickness, which indicate the great advantages in practical applications of organic solar cells (OSCs).

2 Results and discussion

2.1 Design, synthesis, and characterization of PYT1

The state-of-the-art polymer acceptors have shown promis-

ing photovoltaic properties (Figure S1 and Table S1), but their E_g^{opt} values are generally too large to suitably match the solar spectrum [7,14,17,24,25,29]. To further redshift the absorption spectrum and achieve a high absorption coefficient, we designed a polymer acceptor named PYT1 (Figure 1(a)). The synthetic routes and chemical structures of the monomers (Scheme S1) and n-type polymer PYT1 as well as their nuclear magnetic resonance (NMR) spectra (Figures S27–S29, S34, S36) are given in the supporting information (Supporting Information online). PYT1 exhibits good solubility in common organic solvents such as chloroform ($CHCl_3$) and *o*-dichlorobenzene (*o*-DCB) at room temperature. The polymer acceptor is thermally stable with a decomposition temperature beyond 304 °C under inert atmosphere (Figure S2). The theoretical calculations were performed by using the density functional theory (DFT) with the B3LYP/6-31G (d,p) basis set (Figure S3). Meanwhile, to get a study of the impact of electrostatic potential (ESP) on the intermolecular interactions and excited states, the averaged ESP distributions of the two molecular models, including dimers of repeat units of PYT1 and dimers of repeat units of PM6, are mapped in Figure 1(b) on their van der Waals surfaces [36]. For PYT1, the chemical groups with strong electronegative atoms like oxygen, nitrogen, and sulfur have negative ESP while most of its conjugated surface has positive ESP. In contrast, PM6 shows negative ESP values on the most part of its conjugated backbone.

The normalized UV-Vis absorption spectra of D and A materials in solution and film state are presented in Figure 1 (c), and the absorption coefficient of the corresponding polymer acceptors (including N2200, PZ1, and PYT1) in film state is displayed in Figure 1(d). The corresponding data are summarized in Table S2. The PYT1 solution displays an absorption maximum at 810 nm, which is red-shifted significantly to 875 nm in the solid film, corresponding to an optical bandgap of 1.42 eV. In comparison with Y5-C20, the absorption spectrum of the PYT1 film is red-shifted by approximately 30 nm. Of note is that the E_g^{opt} of PYT1 (1.42 eV) is smaller than those of benchmark polymer acceptors, including N2200 (1.47 eV) [37,38] and PZ1 (1.55 eV) [26] as well as other highly efficient acceptors [14,23,24]. In addition, the most significant absorption feature of PYT1 is the maximum absorption coefficient of 9.79×10^4 cm^{-1} (at 800 nm, Figure 1(d)) in the solid state, which is higher than those of N2200 (3.84×10^4 cm^{-1}) and Y5-C20 (7.48×10^4 cm^{-1}). More importantly, PYT1 shows complementary absorption with that of the polymer donor PM6 (Figure 1(c)), which ensures good harvesting of solar light in solar cells. Besides, we estimated the lowest unoccupied molecular orbital (LUMO) and HOMO energy level of PYT1 and Y5-C20 materials (Figure 1(e) and Figure S4), which are −3.92 and −5.69 eV, respectively, for PYT1 and −3.88 and −5.75 eV, respectively, for Y5-C20. Obviously, the electronic energy levels of PYT1 as acceptor also match well with that of the PM6 donor, showing a low D-A HOMO energetic energy offset (ΔE_{HOMO}=0.22 eV). Of note

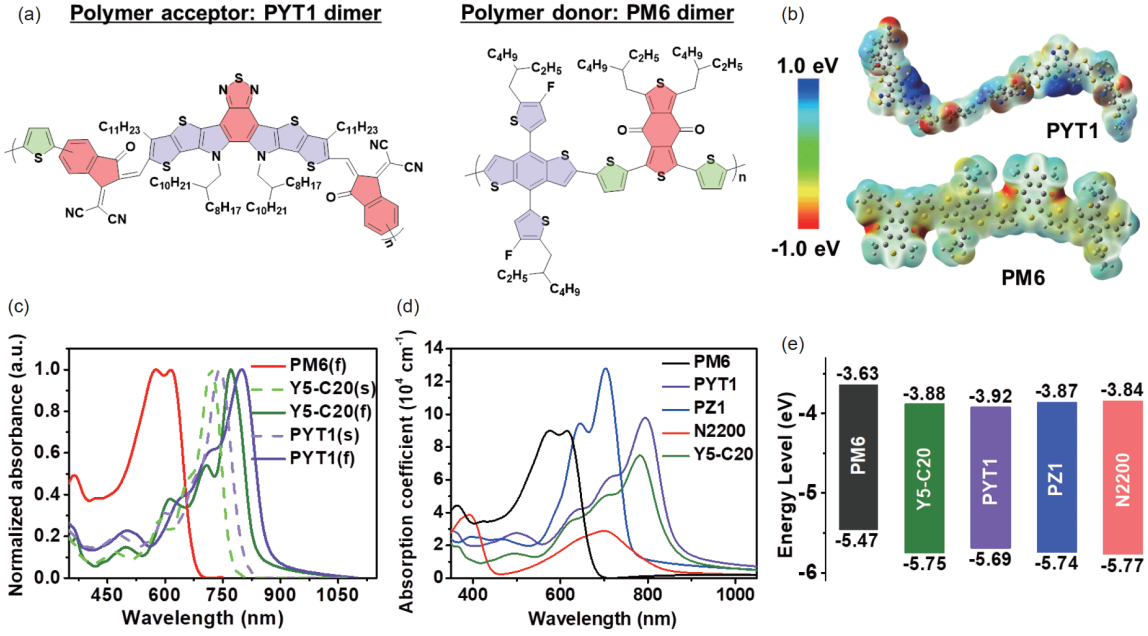

Figure 1 Molecular structures and ESP distributions as well as optical and electrochemical properties of the materials. (a) Molecular structures of PYT1 and PM6. (b) The DFT ESP distributions from PYT1 and PM6, red color indicates a greater negative charge, while blue color indicates positive charges. The sidechains of PYT1 and PM6 are replaced with methyl groups. (c) Optical absorption spectra of polymers PM6 and PYT1 and SMA Y5-C20 in a diluted solution and as thin film. (d) The absorption coefficient of the acceptors N2200, PZ1, PYT1 and Y5-C20 and PM6 donor in film state. (e) Energy level diagram of polymers PM6, N2200, PZ1, and PYT1 (color online).

is that the ΔE_{HOMO} is determined by the HOMO energies of the donor and the acceptor ($\Delta E_{HOMO}=E_{HOMO,D}-E_{HOMO,A}$) [39]. The small ΔE_{HOMO} generally results in a reduction in non-radiative recombination loss and can boost the V_{OC} of all-PSCs with a powerful driving force for the charge separation at the bulk interface [39].

2.2 Photovoltaic performance of all-PSCs

To evaluate PYT1 as an acceptor for all-PSCs, we fabricated the PM6:PYT1 solar cells based on the typical device configuration consisting of a indium tin oxide (ITO)/poly(3,4-ethylene dioxythiophene)poly(styrene sulfonate) (PEDOT:PSS)/active layer/perylene diimide functionalized with amino N-oxide (PDINO) [40]/Al. The details of device fabrication procedures are described in the supporting information (Supporting Information online). In addition, the detailed photovoltaic performance is shown in Figure S5–S7 for the investigated PM6:PYT1 devices, and the detailed photovoltaic parameters are listed in Tables S3–S5. The current density-voltage (*J*-*V*) curves of the corresponding best-performing all-PSCs are plotted in Figure 2(a). On the basis of a 1:1.2 wt% blend ratio, all-PSCs based on the as cast PM6:PYT1 blend exhibit high PCEs of 11.40% (V_{OC}= 0.931 V, J_{SC}=20.87 mA cm^{-2}, FF=58.71%), which is obtained for cells without solvent additives and post-annealing treatments. Here the processing additive 1-chloronaphthalene (CN), successfully used into some all-PSCs [14,25,28], was also employed to significantly improve the efficiency of PM6:PYT1 solar cells in this work. As shown in Figure 2(a) and Table 1, with the addition of 0.5 vol% CN, J_{SC} increased to 21.50 mA cm^{-2}, and the FF increased to 66.66%, which resulted in a record high PCE of 13.43%. It is much higher than the reported PCE values of the NDI- and

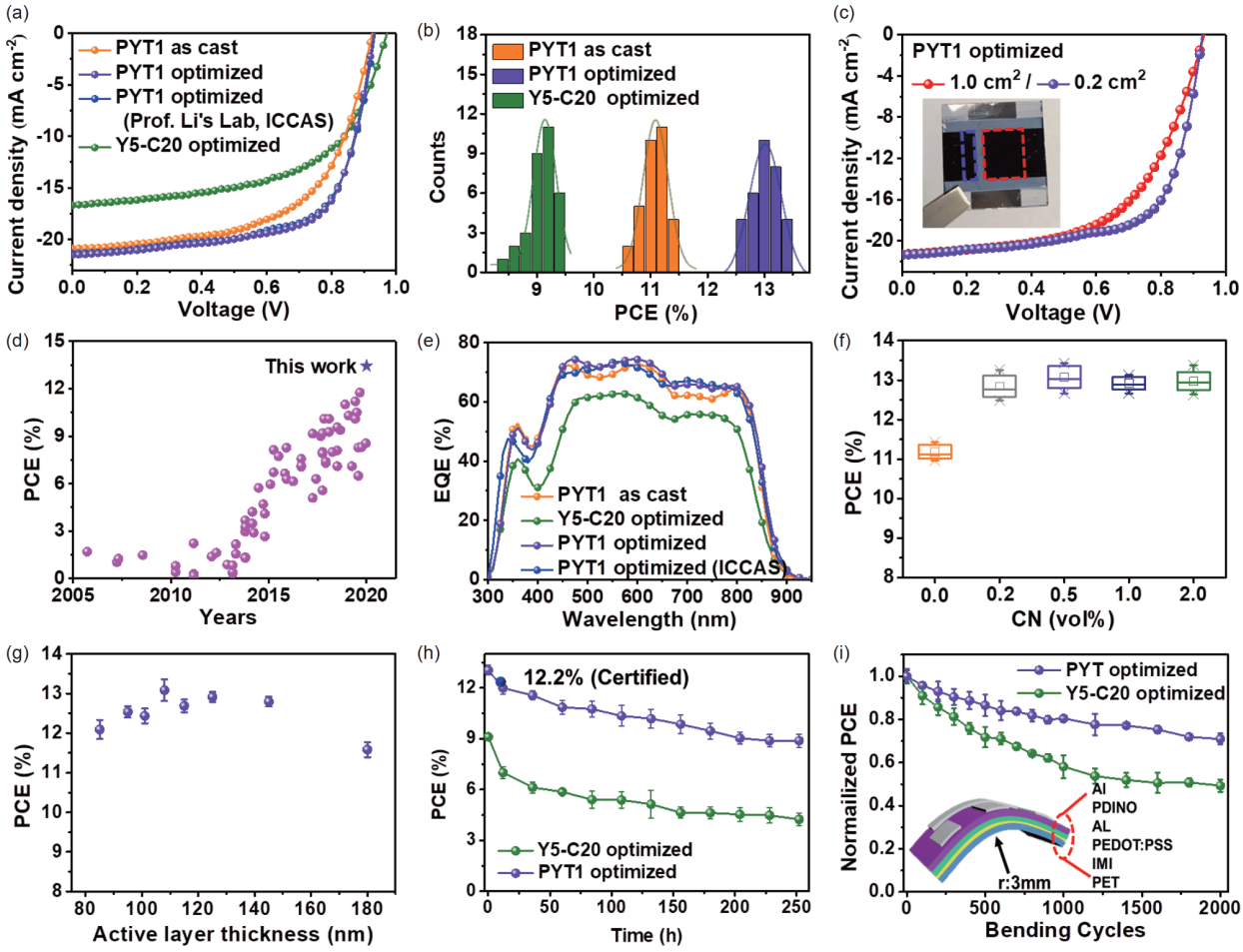

Figure 2 Photovoltaic performance of devices based on different material combinations. (a) *J*-*V* characteristics for devices based on PM6:acceptor tested at Wuhan University and Institute of Chemistry Chinese Academy of Sciences (ICCAS). (b) Histograms of the PCE counts for 32 individual devices based on the corresponding system. (c) *J*-*V* characteristics for devices based on the active layer areas of 0.2 and 1.0 cm^2, respectively. (d) The plots of the PCE *versus* years for the efficient all-PSCs reported in the literature. (e) EQE curves of the corresponding PM6:PYT1 and PM6:Y5-C20 devices. (f) Plots of PCE against CN concentrations for the OSCs based on PM6:PYT1 blends. (g) Plots of PCE against active layer thickness for the OSCs based on PM6:PYT1 blends processed from CN-added solutions, the PCE values are obtained from eight devices for each point. (h) Variation of normalized average PCE losses over 252 h storage for the optimized PM6:PYT1 and the optimized PM6:Y5-C20 devices measured in a dry nitrogen atmosphere. (i) Normalized PCE for the relevant flexible devices with different bending cycles. The inset shows the schematic image of bending cycles with bending radius of 3 mm (color online).

Table 1 Summary of photovoltaic parameters of the OSCs based on PM6:acceptor, measured under the illumination of AM 1.5 G at 100 mW cm^{-2}

Blends	Area (cm^2)	V_{OC} (V)	J_{SC} (mA cm^{-2})	$J_{SC,EQE}$ [f] (mA cm^{-2})	FF (%)	PCE_{max} (PCE_{avg} [g]) (%)
PM6:PYT1 [a]	0.04	0.931	20.87	19.94	58.71	11.40 (11.11±0.21)
PM6:PYT1 [b]	0.04	0.938	21.50	20.81	66.66	13.43 (13.02±0.22)
PM6:PYT1 [c]	0.046	0.931	21.41	20.35	66.72	13.30 (13.04±0.21)
PM6:Y5-C20 [d]	0.04	0.970	17.18	16.52	56.51	9.42 (9.11±0.24)
PM6:PYT1 [b]	0.2	0.935	21.39	20.57	66.53	13.31 (12.96±0.31)
PM6:PYT1 [b]	1.0	0.934	21.33	20.31	57.40	11.43 (11.29±0.11)
PM6:PYT1 [e]	0.02202	0.932	20.33	–	64.40	12.20

a) As-cast devices. b) With CN (0.5%, *v*/*v*) as additive and thermal annealing at 110 °C for 10 min (the optimized condition). c) Devices with an area of 0.046 cm^2 are fabricated at the optimized condition and measured at ICCAS (Prof. Li's group). d) Thermal annealing at 100 °C for 10 min (the optimized condition). e) The device with an active area of 0.046 cm^2 was certified at the optimized condition by the National Institute of Metrology (NIM) in Beijing, China. A non-refractive mask with certified area of 2.202 mm^2 was used for certification of the 0.046 cm^2 device. f) $J_{SC,EQE}$ represents the integrated current density obtained from EQE spectra. g) The average PCE values with standard deviations were obtained from 32 individual devices based on the 0.04 cm^2 photoactive layers, and 4 individual devices based on the 0.046, 0.2 and 1.0 cm^2 photoactive layers, respectively.

FREA-based all-PSCs (Figure S1) [12,14,25,26,28,29]. Of note is that a 13.30% PCE was also achieved in the Institute of Chemistry Chinese Academy of Sciences (ICCAS), thus demonstrating consistency in the results. Besides, we also fabricated the different PM6:Y5-C20 conventional devices. The detailed photovoltaic performance is provided in Figure S8 and the corresponding photovoltaic parameters are summarized in Table S6. The optimal PSCs with small molecule Y5-C20 as acceptor, which is the key building block of PYT1, showed a best PCE of 9.42% (V_{OC}=0.970 V, J_{SC}= 17.18 mA cm^{-2}, FF=56.51%). Figure 2(b) further presents the statistical photovoltaic metrics and PCE histogram obtained from the relevant devices, which further indicates the good reproducibility of the photovoltaic performance of the corresponding PSCs.

Due to the special advantages of the PM6:PYT1 system as mentioned above, we further manufactured large-area all-polymer OSCs with active areas of 0.2 and 1.0 cm^2, as shown in Figure 2(c). The best performances of the 0.2 cm^2-based devices reach a higher PCE of 13.31% compared to the 1.0 cm^2-based devices (11.43% PCE, Figure 2(c) and Table 1), mainly attributed to different FF values (57.40% for the 1.0 cm^2-based device and 66.53% for the 0.2 cm^2-based device, respectively). In addition, the J_{SC} values calculated by integrating the external quantum efficiency (EQE) data (Figure S9) agree well with those obtained from the *J*-*V* measurements within 5% mismatches. Besides, we also sent the best performing device to the National Institute of Metrology, China (NIM), for certification to verify our photovoltaic results. As provided in Figure S10 and Table S1, a certified PCE of 12.20% can be recorded, to best of our knowledge, this is the highest certified PCE in the all-polymer solar cells. Compared with the best PCE tested in the laboratories, the NIM certified PCE is slightly lower, which is mainly due to the performance degradation of the encapsulated devices. In this work, many factors, including the use of unstable PDINO layer, the conventional structure, the device packaging and long transportation, can cause the corresponding degradation of device performance. Notably, Figure 2(d) shows the plots of PCE values *versus* years for the reported efficient all-PSCs in literatures. The corresponding statistical photovoltaic parameters are listed in Table S7. It can be seen from the figure that the PM6:PYT1 all-PSC has the highest PCE of 13.43%, which is benefitted from the design strategy of acceptor PYT1 with a narrow bandgap and a high absorption coefficient as well as a low energy loss as discussed in below. Obviously, PYT1 possesses great superiority in photovoltaic performance, which will lead to a bright future for the potential application of all-PSCs.

The cells which contained PM6 and PYT1 had a slightly lower V_{OC} (0.931–0.938 V) than the cells which contained Y5-C20 (0.970 V), which is consistent with the low-lying LUMO energy level of PYT1 (Figure 1(e)) and the narrow optical bandgap (Figure 1(c)). To elucidate the higher J_{SC} in the optimized PM6:PYT1 devices as compared to the optimized PM6:Y5-C20 devices, we firstly analyzed the blend-film absorption (Figure S11). Similar to the neat-film absorption of PYT1 (Figure 1(c)), the redshifts are also present in the corresponding blend films, which partly contribute to the J_{SC} enhancement (see the EQE response, Figure 2(e)). The EQE values of the PYT1-based devices were greatly enhanced in the wavelength ranges of 600–900 nm corresponding to the absorption of the PYT1, which can be ascribed to the narrow optical bandgap and high absorption coefficient of the PYT1 film over the previously reported polymer acceptors [17,18,25,26]. Apart from the J_{SC}, the FF values in the optimized PYT1- and Y5-C20-based devices also showed a huge difference (66.66% for PM6:PYT1 device and 56.51% for PM6:Y5-C20 device, respectively). In short, these photovoltaic parameters of the corresponding devices further confirm the advantages of PYT1 as a polymer acceptor in the all-PSCs, and verify the success of our synthetic strategy.

The other CN concentrations also lead to improved device performance, but a slightly lower level than that of 0.5 vol% CN (Figure S6 and Table S4). Notably, the corresponding devices can deliver high PCEs of over 13% with a broad CN additive contents (from 0.2% to 2.0%; Figure 2(f)). The results suggest that the PM6:PYT1 system has high composition tolerance of CN additives, which shows the similar trends with other PM6-based all-PSCs [14,25,28]. Of note is that the addition of CN additives did not significant improve the photovoltaic performance of PM6:Y5-C20 system (Figure S8). In addition, benefiting from these high and balanced charge carrier mobilities tested by the space charge limited current (SCLC) model (Figures S12, S13, and Table S8), the optimized PM6:PYT1 blend exhibited good device performance at varied thicknesses (85–180 nm; Figure S7 and Table S5), with an optimal performance at 108 nm and a high average PCE of 11.53% maintained at a 180 nm thicknesses (Figure 2(g)). It should be noted that a further increase in active layer thickness while maintaining high device performance is not available due to the solubility limitations of PYT1 in chloroform solvent. The desirable device reproducibility and the less sensitivity to the thickness and CN additive content are great advantages for potential applications of this PM6:PYT1 photovoltaic system.

Our results are very interesting since PM6:PYT1-based device efficiency improves significantly, resulting from the polymerization of molecular acceptor Y5-C20. This drives us to further explore the stability issues of the relevant devices and compare the photovoltaic performance of PYT1 and Y5-C20-based systems. Based on this point, we explored the long-time stored stability of the PYT1 and Y5-C20-based devices tested in the nitrogen glovebox at room temperature. Figure 2(h) shows the changes of the recorded PCEs of the optimized devices of PM6:Y5-C20 and PM6:PYT1 system, and Figure S14 exhibits their relative degradation trends of photovoltaic parameters. The Y5-C20-based devices experienced an initial loss of performances in a short period of hundreds of hours, with approximately 46% of their initial efficiencies retained (Figures S14(d) and S15(a)). The PYT1-based devices also showed an obvious reduction in PCE and kept 76% of their initial efficiencies within the same time frame (Figures S14(d) and S15(b)). The results so far suggest that the PM6:PYT1 devices possess better storage stability. Noteworthily, the corresponding results also partly confirm the availability of the NIM certified PCE, as provided in Figure 2(h). We also investigated the light soaking stability of solar cell devices based on PYT1 and Y5-C20-based systems under simulated one sun illumination in the nitrogen glovebox. As shown in Figure S16, both PM6:Y5-C20 and PM6:PYT1-based devices exhibit similar stability under continuous illumination with obvious PCE degradation. After light-soaking for 252 h, the average PCE of PM6:Y5-C20-based optimized devices decays from 9.09% to 4.89%; the average PCE of PM6:PYT1-based optimized devices decays from 13.05% to 6.72%, preserving only 54% and 52% of their original values, respectively. The difference in storage stabilities of these two systems might be mainly due to the synergistic effects of the morphology evolution and interface attenuation. It should be noted that the relevant interface materials, especially for PDINO, can significantly alter the storage and light-soaking stabilities of the most of devices, quantitative evaluation of such photostability performance of the corresponding photovoltaic systems are beyond the scope of the present work.

In order to compare the mechanical stability between the flexible all-PSCs based on the optimized PM6:PYT1 and PM6:Y5-C20 active layers, their performances depending on bending cycles were investigated. Figure 2(i) exhibits the normalized PCEs of the PM6:PYT1 and PM6:Y5-C20 devices as a function of bending cycles with a radium of 3 mm. The PCEs of the PM6:PYT1 and PM6:Y5-C20 devices maintained approximately 71% and 49% of the corresponding initial performances, respectively, after 2,000 bending cycles. This result indicates that the polymerization of Y5-C20 can significantly increase the mechanical stability of the relevant active layer in terms of bending. Accordingly, these results indicate that the PYT1-based all-PSCs possess good photovoltaic stability because of the active layer morphology forming a bicontinuous interpenetrating network with proper phase-separated domains, which will be discussed below.

2.3 Structural and morphological properties of active layers

The promising device results drive us to investigate the structure details of relevant blends, which was accomplished by using two-dimensional (2D) grazing incidence wide-angle X-ray diffraction (GIWAXS), atomic force microscope (AFM) and grazing-incidence small-angle X-ray scattering (GISAXS) measurements. The thin-film crystallization at the nanoscale is investigated by GIWAXS measurement. Figure 3(a–c) presents two-dimensional GIWAXS patterns of pure PM6, PYT1, and Y5-C20 thin films, respectively. And the relevant crystallographic parameters of these films are summarized in Table S9. As observed from Figure 3(a) and Figure S17, the simultaneous appearance of (100) lamellar diffraction at q=0.286 Å^{-1} (lattice spacing (d)=21.96 Å, coherence length (CCL)=105.91 Å) and (010) π-π diffraction along with both in-plane (IP) at q=0.64 Å^{-1} (d=9.81 Å, CCL=94.15 Å) and out-of-plane (OOP) directions at q=1.683 Å^{-1} (d=3.73 Å, CCL=22.43 Å), suggests that PM6 adopts the bimodal distribution of both face-on and edge-on crystallites with respect to the substrate. On the other hand, as seen in Figure 3(b, c), the lamellar (100) peak is located at 0.271 Å^{-1} (d=23.17 Å, CCL=62.0 Å) and the π-π stacking

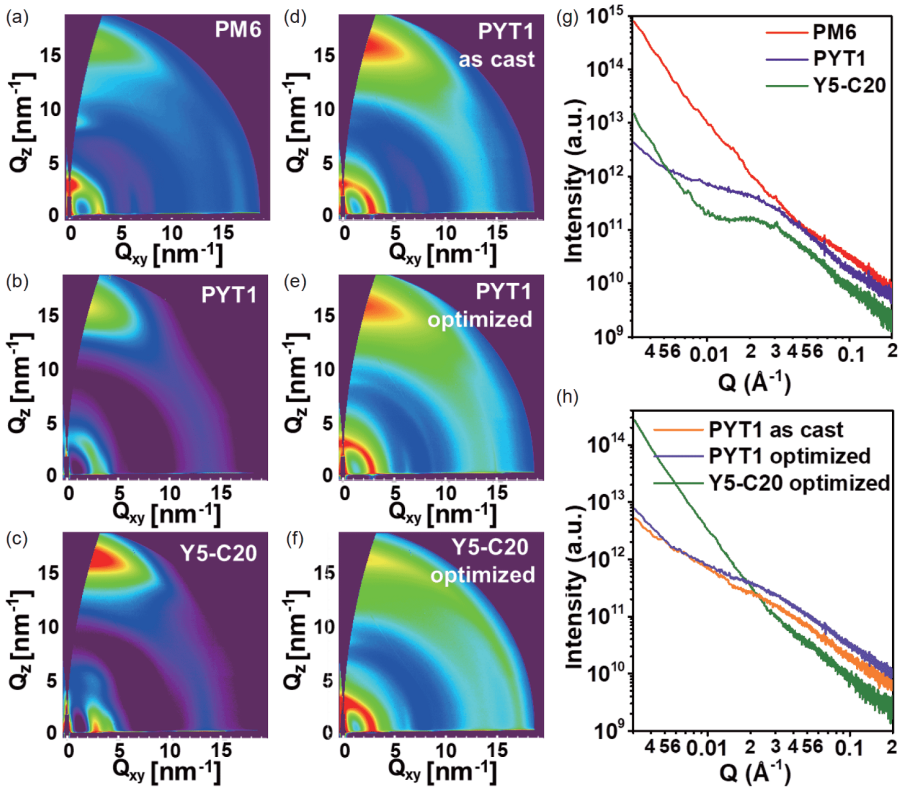

Figure 3 Morphological characteristics of active layers. GIWAXS patterns for pure films of (a) PM6, (b) PYT1, (c) Y5-C20, and the PM6:acceptor blend films of (d) PYT1 (as cast), (e) the optimized PYT1 (0.5% CN), (f) the optimized Y5-C20. (g) Relevant neat films and (h) binary blends 1D GISAXS along the in-plane direction to represent lateral domain distribution. All GISAXS data were taken at 0.13°, where the scattering signal maximizes (color online).

(010) peak is observed at 1.641 $Å^{-1}$ (d=3.83 Å, CCL= 19.4 Å) for the neat PYT1 film, while that for the lamellar (100) of Y5-C20 film is at 0.28 $Å^{-1}$, with a lattice spacing of 22.42 Å (CCL=78.5 Å). It suggests that crystallites in PYT1 and Y5-C20 films adopt face-on orientation, evidenced by the (100) lamellar diffraction along the IP direction and (010) π-π diffraction along OOP direction.

Next, we investigated the different blend active layers with PM6 as a donor using GIWAXS to shine light on the morphological changes in blends upon changing additive or acceptor. As shown in Figure 3(d, e), the similar q position of (100) and (010) peaks and CCL (Table S10) based on the as cast PM6:PYT1 films and the optimized PM6:PYT1 films (0.5 vol% CN), indicating that the application of 0.5 vol% CN does not bring in a considerable change in crystallite formation. A closer look at Figure 3(d, e) unravel that the (300) lamellar diffraction from the optimized PM6:PYT1 has more isotropic pole angle distribution than that the as cast devices. This suggests that the incorporation of 0.5 vol% CN only impacts the preferential orientation of PM6 crystallites at the nanoscale, as shown in Figure S18. Crystallite orientation distribution (COD) analysis was performed based on the pole angle distribution of PM6 lamellar (100) diffraction and the results were presented in Figure S19. Bimodal distribution of face-on and edge-on can be clearly seen from Figure S19(a, b). The addition of CN is helpful for the construction of an interpenetrating structure and efficient transport path for electrons to the electrode in the blend. Unexpectedly, blending PM6 with Y5-C20 brings up a (010) π-π with wide-spread pole angle distribution, which was not observed in either pure PM6 or Y5-C20 films. The crystallite orientation distribution shown in Figure S19(c) also indicates that blending with Y5-C20 largely reduce the population of face-on crystallites. The relatively least face-on preference of PM6:Y5-C20 film, evidenced by the least anisotropic scattering ring of (010) π-π, may be the reason contributing to unsatisfactory device performance.

Mesoscale domain distribution has been probed by GISAXS measurement. The scattering patterns of pure materials and blends parallel to the substrate are demonstrated in Figure 3(g, h), respectively. From Figure 3(g), the lateral domain distributions originating from electron density fluctuation of three pure material thin films are considerably different. To quantify domain distribution, the model-free Guinier analysis was applied within the low-q region of GISAXS data and the fitting results were summarized in Figure S20. The low-q region scattering profiles of all three pure films can be fitted by two separate linear region in the ln ($I(Q)$)-Q^2 plots, indicative of hierarchical structure. According to Guinier analysis, all three pure thin films consist

of domains with larger and smaller radius of gyration, respectively. Note is that values of radius of gyration for larger and smaller domains were summarized as $R1$ and $R2$ in Figure S20. Considering the hard X-ray is sensitive to mass-thickness contrast, which potentially features the scattering from film thickness variation or surface roughness, AFM images were taken to rule out the possibility of misinterpreting the GISAXS data. As shown from the AFM images (Figure S21), all three thin films show the similar surface roughness and smooth thickness variation, thereafter validating that our GISAXS data truly probes the mesoscale phase behaviors of the investigated materials.

As with the pure materials, blends were also probed by GISAXS, and the scattering profiles parallel to the substrate are demonstrated in Figure 3(h). Similar with pure films, all blends also exhibit hierarchal structures induced by Guinier analysis. Interestingly, the radius of gyration of both larger and small domains of the optimized PM6:PYT1 film are effectively reduced compared to the as-cast PM:PYT1 film. As indicated from Figure S20, the larger domain reduces from 47 to 36 nm and the smaller domain reduces from 21 to 14 nm. The reduced domain size close to exciton diffusion length in organic photovoltaic materials after CN treatment contributes to better J_{SC}. Besides, the stronger overall scattering intensity (after film thickness and X-ray footprint normalization) of PM6:PYT1 after CN treatment implies higher domain purity which further correlates well with the improved device performance, collectively contributing to a ~12% enhancement in FF (58.71% *vs.* 66.66%) and ~18% enhancement in PCE (11.40% *vs.* 13.43%) in the corresponding all-PSCs. The preferable molecular orientation was beneficial for charge transport and collection and resulted in high J_{SC} and high FF in devices. Although the optimized PM6:Y5-C20 film, along the direction parallel to substrate, generates a GISAXS profile with resemblance of optimized PM6:PYT1 film, the inferior crystallite organization suggested by GIWAXS analysis leads to suppressing charge carrier transporting and leading to unnecessary carrier recombination, which will be further discussed in the next section [41]. The surface roughness of mesoscale domains was also quantified by Porod analysis and illustrated in Figure S22. In the $\ln(I(Q))$-$\ln(Q)$ plot, a smooth interface generates a fast decay with a slope of −4, while any fractural surface slows down the decay with less slope [42]. From Figure S22, with CN treatment, a slightly steeper slope can be seen in the PM6:PYT1 film, indicative of smoother interface.

2.4 Optimized exciton and carrier dynamics to improve J_{SC} and FF

The blend morphologies and D/A interfaces determine the fundamental processes associated with the conversion of light (photons) into the current (extracted charges at electrodes). To better understand the effect of morphological variation on device performance, we studied the exciton dynamics, charge generation, transport, and collection processes in these three blends by employing steady-state and transient spectroscopic techniques. The photoluminescence (PL) of blend films is firstly recorded to detect charge generation at the interface of thin films. PL spectroscopy (Figure 4(a)) finds quenching efficiencies of approximately 80% for PM6:PYT1 blends processed without and with 0.5 vol% CN and 74% for the optimized PM6:Y5-C20 blend. The higher PL quenching in the PYT1-based blends indicates that more excitons are available for charge generation. Interestingly, the PL intensity of PM6:PYT1 blend increases slightly by adding 0.5 vol% of CN, as seen in Figure 4(a), suggesting that the interface area between PM6 and PYT1 decreases slightly. In contrast, the exciton dissociation of PM6:Y5-C20 blend can be a limiting factor for the lower photocurrent of the devices (Figure 2(a)). Of note is that these PL experiments also confirm the above-mentioned morphology characteristics of the blends.

In order to provide more insight into the reasons for the observed performance trends, we also studied the charge photo-generation of relevant devices by examining the photocurrent at the saturation point where the internal field is large enough to sweep out all carriers to the electrodes prior to recombination. The trend of the photocurrent density (J_{ph}), obtained as the difference between the current under one sun illumination and that flowing in the dark, is plotted in Figure 4(b) *versus* the effective voltage (V_{eff}, $V_{eff}=V_0-V$) for the devices with different active layers. Here V_o is the compensation voltage at which J_{ph} is zero, and V is the external applied voltage [43]. As exhibited in Figure 4(b), the J_{sat} values at V_{eff}=5 V are 24.27 and 24.67 mA cm^{-2} for the as cast PM6:PYT1 and the optimized PM6:PYT1devices, respectively. Differently, a voltage-dependent behavior of J_{ph} was obviously observed for the PM6:Y5-C20 devices, indicating the high dependence of the electric field on charge carrier transport, which is consistent with the reduction in J_{SC} and FF [43]. Furthermore, the J_{ph}/J_{sat} ratio is used to determine the overall efficiencies of exciton and charge collections. Among these three devices, the optimized PM6:PYT1 device shows the highest value of 96.3% under short-circuit and maximum output power condition, revealing the more efficient processes of exciton dissociation and charge collection in the blend. Of note is that the J_{ph} at the same V_{eff} is 22.05 mA cm^{-2} for the PM6:Y5-C20 device. Obviously, just a small portion of the large J_{sc} losses of PM6:Y5-C20 device compared to the PYT1-based devices can be explained by the poor optical absorption of PM6:Y5-C20 blend (Figure S11). Thus, the major loss in J_{SC} of PM6:Y5-C20 device may be attributed to the unbalanced and/or poor charge carrier transport as well as increased non-geminate

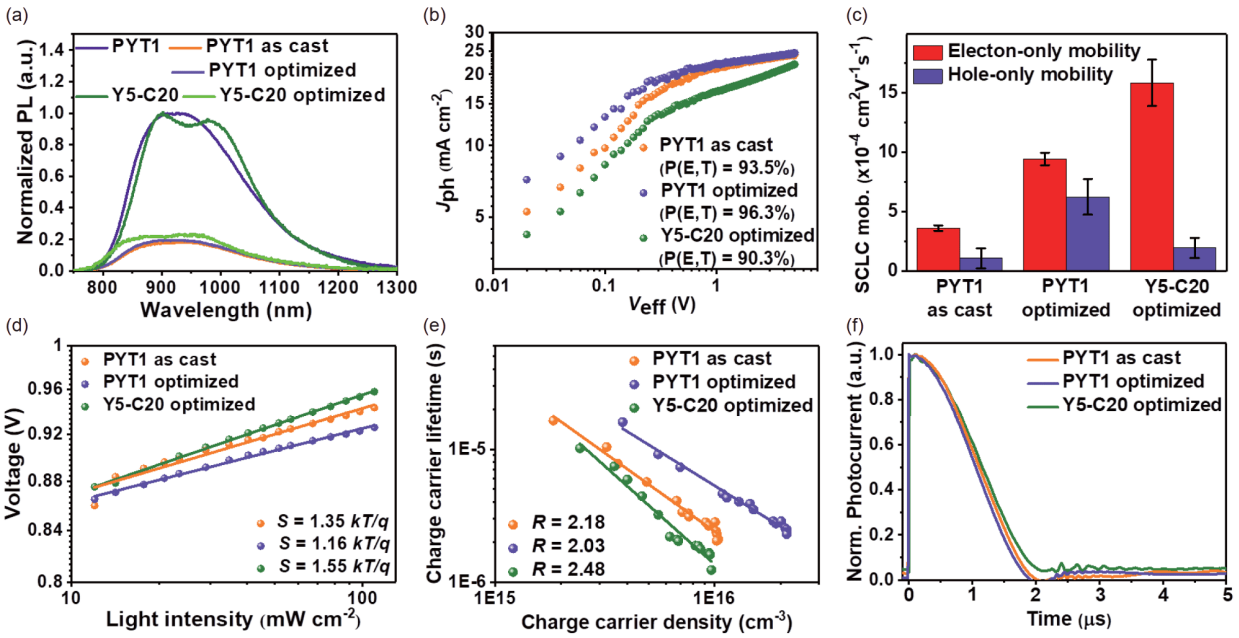

Figure 4 Charge generation, transport, extraction and recombination. (a) PL spectra of the pristine acceptors (PYT1 and Y5-C20) and blended films. The intensities are corrected by their absorptions at the excitation wavelength (639 nm). The quenching efficiency is calculated by equation of (Φ_q=(I_0−I)/I_0), where I_0 is the PL intensity of neat films, I is the PL intensity of blend films. (b) Characteristics of the photocurrent density *versus* effective voltage (J_{ph}-V_{eff}). (c) The hole and electron mobilities of the devices based on the corresponding blends. (d) Measurement of V_{OC} *versus* light intensity for the devices. (e) Charge carrier lifetime τ, obtained from TPV, as a function of charge density n, calculated from CE under V_{OC} conditions (from 0.15 to 2.50 suns). The dashed lines represent linear fits of the data. (f) Normalized TPC data for the relevant devices. The illumination pulse intensity was 150 mW cm^{-2} (light pulse of 50 μs) (color online).

recombination mainly resulting from an unfavorable blend morphology.

To gain insight into the charge transport properties of relevant blends, SCLC spectroscopy was used to map out the charge carrier mobilities in pristine and blended films. The hole and electron mobilities of the relevant pristine and blend films were investigated by analyzing the *J*-*V* characteristics of single-carrier devices (Figure S12 for hole only device and Figure S13 for electron only device), and their results are summarized in Table S8. The fitting to the experimental results reveal that the electron mobilities of the pristine films are 3.20×10^{-4} cm^2 V^{-1} s^{-1} for PYT1 and 4.11×10^{-4} cm^2 V^{-1} s^{-1} for Y5-C20. The pristine PYT1 film shows lower electron mobility, which is consistent with the fact that it has less intermolecular interactions and molecular ordering than Y5-C20 (Figure 3(b, c)). The electron mobility of PM6:Y5-C20 blend is 1.58×10^{-3} cm^2 V^{-1} s^{-1}, which is significantly higher than those of the as cast and optimized PM6:PYT1 blends (3.62×10^{-4} and 9.43×10^{-4} cm^2 V^{-1} s^{-1}, respectively). In addition, the average hole mobility of PM6:Y5-C20 blend is 1.95×10^{-4} cm^2 V^{-1} s^{-1}, which is slightly higher than that of the as cast PM6:PYT1 blend (1.08×10^{-4} cm^2 V^{-1} s^{-1}), but approximately three times lower than that of the optimized PM6:PYT1 blend (6.24×10^{-4} cm^2 V^{-1} s^{-1}). As shown in Figure 4(c), the unbalanced electron and hole mobilities in the optimized PM6:Y5-C20 (μ_h/μ_e=0.12) and PM6:PYT1 (μ_h/μ_e=0.30) systems indicate that their blends are transport-limited systems, leading to a square-root behavior in J_{ph} for the relevant devices with low FF values as aforementioned in the Figure 2 (a). In contrast, the more balanced charge transport properties in the optimized PM6:PYT1 active layer with a μ_h/μ_e of 0.66 suggest that charge carriers can be transmitted more efficiently, which is also consistent with the better blend morphology as discussed above.

To get insight of the influence of blend morphology on the charge recombination, the correlations between V_{OC} or J_{SC} and light intensity (P_{light}) were studied [43], as provided in Figure 4(d) and Figure S23, respectively. The relationship between the J_{SC} and P_{light} can be interpreted based on the formula, $J_{SC}\propto P_{light}^{\alpha}$, in which the exponential factor α denotes the degree of bimolecular recombination. As shown in Figure S23, the similar α values close to unity indicate negligible bimolecular recombination during sweep-out in the corresponding devices [43]. The optimized PM6:PYT1 blend shows a small slope of 1.16 kT/q (where k is the Boltzmann's constant, T is the temperature in Kelvins, and q is the elemental charge), while the as cast PM6:PYT1 blend exhibits a large slope of 1.35 kT/q. The results indicate the more balanced charge transport and less trap-assisted recombination in the optimized PM6:PYT1devices, thus leading to improvements in J_{SC} and FF and resulting in an enhancement in the PCE of the all-PSCs. As compared to the as cast PM6:PYT1 devices, a higher slope of 1.55 kT/q was

found (Figure 4(d)), implying the serious trap-assisted charge recombination in the optimized PM6:Y5-C20 devices. In addition, in order to directly figure out the situations of carrier recombination in these blends, we combined the transient photovoltage (TPV) and charge extraction (CE) techniques to yield the charge carrier lifetime τ (Figure S24) as a function of charge carrier density n (Figure S25) under open-circuit conditions, $\tau(n)$. Here, a non-geminate recombination order R (R=λ+1) can be calculated *via* the equation of $\tau = \tau_0(n_0/n)^{\lambda}$, where τ_0 and n_0 are constants and λ is the so-called recombination exponent [5]. As shown in Figure 4(e), a lower recombination order value (R=2.03) for the optimized PM6:PYT1 device as compared to the as cast PM6:PYT1 device (R=2.18) and the optimized PM6:Y5-C20 device (R=2.48) can be found, suggesting that such material combination and morphology optimization *via* CN additives yield overall improved J_{SC} and high FF values. In contrast, poor morphology caused by a large domain with less purity in PM6:Y5-C20 blend leads to a strong charge recombination; thus a poor FF of 56.51% is observed.

We also evaluated the influence of the different morphologies on the charge collection efficiency and the dwell time of charges in the active layer prior to charge extraction at the electrodes. Figure 4(f) exhibits the charge extraction of the relevant devices at J_{SC} condition measured by transient photocurrent (TPC) measurements. The extraction time of the corresponding devices were extracted to be τ=0.73 μs for the as cast PM6:PYT1, τ=0.62 μs for the optimized PM6:PYT1, τ=0.81 μs for the optimized PM6:Y5-C20, respectively. Among them, the optimized PM6:PYT1 device showed the shorter extraction lifetime, suggesting that photogenerated carriers are extracted more efficiently in this device than the other two systems. Of note is that the trend of extraction lifetime calculated from TPC curves is almost consistent with the trend of carrier lifetime measured by TPV measurements (Figure S24). The shorter carrier lifetime in the optimized PM6:PYT1 device may be ascribed to less charge recombination and fewer traps within the blend supported by the above-discussed morphology characterizations and the light intensity dependence of the V_{OC} (Figure 4(d)). These results also imply that the difference in J_{SC} and FF observed in these devices is not only a consequence of different non-geminate recombination rates, but also the rate of charge extraction. Overall, the carrier recombination dynamic analysis coupled with the charge carrier mobilities and exciton dissociation properties finally underpin the complex morphology as outlined above and give detailed insight into subtle mechanisms being responsible for device parameters.

2.5 Energy loss analysis in all-polymer solar cells

In order to further highlight the advantage of polymer acceptor PYT1, the correlations of eV_{OC} *versus* E_g^{onset}, and E_{loss} *versus* PCE values of the efficient all-PSCs reported so far are shown in Figure 5(a, b), respectively. The corresponding statistical photovoltaic parameters are presented in Table S7. In the reported literature, the E_{loss} of all-PSCs is mainly concentrated in 0.55–0.80 eV. Only a few of the OSCs based on active layer materials with the wide absorption spectra and matched energy levels have been reported to maximize the V_{OC} value and minimize the E_{loss} value simultaneously. Notably, it can be seen from the figures that the PYT1-based PSCs has the highest PCE (13.43%) with the minimum energy loss (an E_{loss} value of 0.47 eV, E_{loss}=E_g^{onset}−eV_{OC}). The less energy loss of PYT1-based system should be ascribed to its improved blend microstructure and reduced radiative and non-radiative energy loss channels that thus lead to an increase in V_{OC}. Obviously, PYT1 exhibits great superiority in both optical absorption and energy loss, which manifests the indispensability of FREAs in OSCs.

Actually, it is very difficult to achieve high PCEs at low E_{loss} in all-PSCs because of the inherent trade-off between V_{OC} and J_{SC}. Here the devices still obtain a high PCE of 13.43% (Figure 2(a)), which is mainly due to the relevant active layer that has a high absorption coefficient, good morphology, as well as the small ΔE_{HOMO} of 0.22 eV (Figure 1(e)). The low ΔE_{HOMO} value can result in hybridization between charge-transfer and lowest donor or acceptor exciton sates, which probably leads to a strong suppression in the non-radiative voltage loss [39]. To further understand the voltage losses in the as cast and optimized PM6:PYT1 blends, we further quantified the energy losses by characterizing Fourier-transform photocurrent spectroscopy (FTPS)-EQE and electroluminescence (EL) spectra in these investigated solar cells (Figure 5(c, d)). The calculation results are summarized in Table S11. Following the Shockley-Queisser (SQ) limit [44,45], the voltage losses ($q\Delta V_{OC}$) can be categorized into three different terms ($q\Delta V_{OC} = E_{gap} - qV_{OC}^{SQ} + q\Delta V_{OC}^{rad} + q\Delta V_{OC}^{non\text{-}rad}$) [46]. The E_{gap} values of the blends (as cast and optimized) obtained were 1.485 and 1.466 eV, respectively, suggesting that these two devices show the same $\Delta E_1 = E_{gap} - qV_{OC}^{SQ}$ with a value of approximately 0.26 eV. Unlike the E_g^{onset}, here the E_{gap} is determined from the intersection point of the EL spectra and absorption spectra of the relevant blends (Figure S26). In addition, it was found that the optimized PM6:PYT1 device showed the smaller $\Delta E_2 = q\Delta V_{OC}^{rad}$ with a value of 0.058 eV and $\Delta E_3 = q\Delta V_{OC}^{non\text{-}rad}$ with a value of 0.211 eV as compared to those of the PM6:PYT1 devices (0.066 and 0.228 eV, respectively). Thus, the optimized PM6:PYT1 blend could effectively reduce radiative recombination, block the non-radiative decay channels, reduce energy loss (from 0.554 eV for the as cast PM6:PYT1 device to 0.528 eV for the opti-

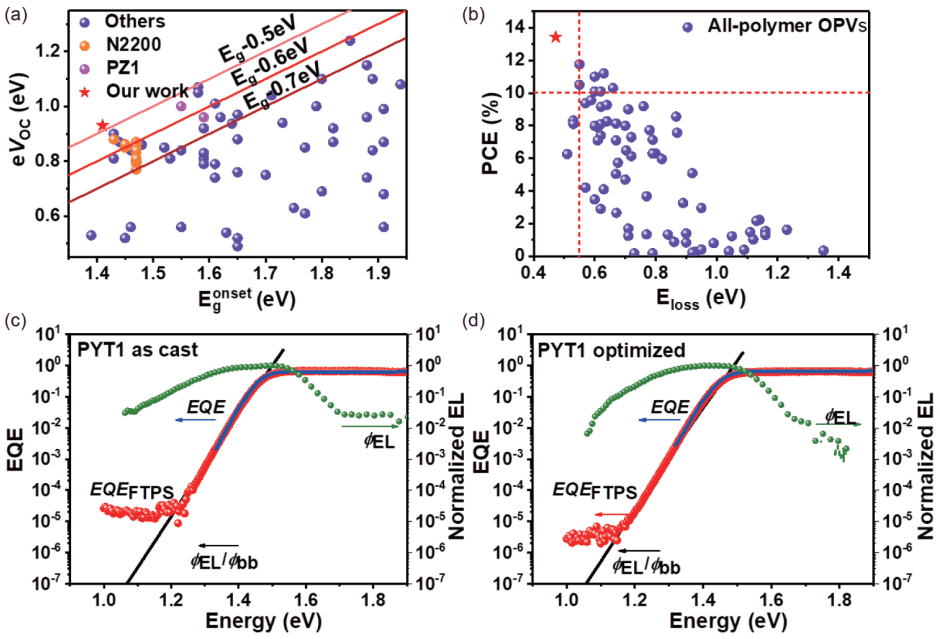

Figure 5 Energy loss analysis in all-PSCs. Plots of (a) eV_{OC} *versus* E_g^{onset} and (b) E_{loss} (E_{loss}=E_g^{onset}−eV_{OC}) *versus* PCE in the various single-junction all-PSCs. Note that E_g is determined from the EQE onset [47], denoted as E_g^{onset}. The vertical line of red dash-dot is the line of E_{loss}=0.55 eV, the horizontal line of red dash-dot is the line of PCE=10%. Semi-logarithmic plots of normalized EL, measured EQE and EQE calculated by FTPS (EQE$_{FTPS}$) as a function of energy for devices based on (c) the as cast PM6:PYT1 active layer and (d) the optimized PM6:PYT1 active layer, wherein a visible charge transport feature is indicated. The ratio of ϕ_{EL}/ϕ_{bb} was used to plot the EQE in the low-energy regime (black line), where ϕ_{EL} and ϕ_{bb} represent the emitted photon flux and the room-temperature blackbody photon flux, respectively (color online).

mized device) and thus improve the V_{OC} of the relevant devices (from 0.931 to 0.938 eV, Table S11), which have also been demonstrated by the above-mentioned physical measurements and are associated with the morphological characteristics. These exciting results further show the important of the polymer acceptor PYT1 in simultaneously reducing energy losses and obtaining high J_{SC} and FF values, forming appropriate interfaces, suppressing unfavorable charge-transfer state and carrier recombination losses.

3 Conclusions

In summary, a π-conjugated polymer acceptor, PYT1, was developed by combining a fused-ring electron acceptor Y5-C20 as the key building block. PYT1 shows improved absorption spectrum (a narrow E_g^{opt} of 1.42 eV) and a high absorption coefficient (9.79×10^{-4} cm^{-1} at 800 nm) as well as high electron mobility of 3.20×10^{-4} cm^2 V^{-1} s^{-1}. When blended with the wide bandgap polymer donor PM6 to fabricate devices, the all-PSCs based on the optimized PM6:PYT1 blend (0.5 vol% CN) show a PCE of 13.43% with a very low energy loss of 0.472 eV, the highest value reported in the literatures to date for the all-PSCs. We also demonstrate that this PM6:PYT1 system has great advantages in potential applications due to its excellent long-term stored and mechanical stability, insensitivity to CN additive contents, and active-layer thickness. In addition, of note is that the photovoltaic performance of the optimized PM6:PYT1 system is significantly improved over the PCEs of 11.40% for the as-cast PM6:PYT1 system and 9.42% for the optimized PM6:Y5-C20 system. Mechanism investigation reveals that such an improvement in the optimized PM6:PYT1 system as compared to the other two devices was mainly due to a more balance between detailed phase separation and material crystallization in combination with the exciting physical dynamics, including the efficient charge generation, balanced charge transport properties, low carrier recombination losses and fast charge extraction in the devices. Overall, the results position PYT1 as a very attractive polymer acceptor material candidate meeting the requirements for potential production significantly better than the small molecule acceptors on one hand. On the other hand, this work indicated that the rational design of FREA structure as a building block is crucial to achieve high-performance polymer acceptors and break through the reported champion PCE of PSCs.

Acknowledgements This work was supported by the National Natural Science Foundation of China (21702154, 51773157), and the opening projects of Key Laboratory of Materials Processing and Mold and Beijing National Laboratory for Molecular Sciences (BNLMS201905). This work was performed in part on the SAXS/WAXS beamline at the Australian Synchrotron, part of ANSTO.

Conflict of interest The authors declare no conflict of interest.

Supporting information The supporting information is available online at http://chem.scichina.com and http://link.springer.com/journal/11426. The supporting materials are published as submitted, without typesetting or editing. The responsibility for scientific accuracy and content remains entirely with the authors.

1 Cui C, Li Y. *Energy Environ Sci*, 2019, 12: 3225–3246
2 Yang J, Xiao B, Tang A, Li J, Wang X, Zhou E. *Adv Mater*, 2018, 31: 1804699
3 Guo J, Min J. *Adv Energy Mater*, 2019, 9: 1802521
4 Yuan J, Zhang Y, Zhou L, Zhang G, Yip HL, Lau TK, Lu X, Zhu C, Peng H, Johnson PA, Leclerc M, Cao Y, Ulanski J, Li Y, Zou Y. *Joule*, 2019, 3: 1140–1151
5 Xu X, Feng K, Bi Z, Ma W, Zhang G, Peng Q. *Adv Mater*, 2019, 31: 1901872
6 Cui Y, Yao H, Zhang J, Zhang T, Wang Y, Hong L, Xian K, Xu B, Zhang S, Peng J, Wei Z, Gao F, Hou J. *Nat Commun*, 2019, 10: 2515
7 Wang G, Melkonyan FS, Facchetti A, Marks TJ. *Angew Chem Int Ed*, 2018, 58: 4129–4142
8 Menke SM, Ran NA, Bazan GC, Friend RH. *Joule*, 2018, 2: 25–35
9 Huang W, Cheng P, Yang YM, Li G, Yang Y. *Adv Mater*, 2018, 30: 1705706
10 Hou J, Inganäs O, Friend RH, Gao F. *Nat Mater*, 2018, 17: 119–128
11 Kang H, Lee W, Oh J, Kim T, Lee C, Kim BJ. *Acc Chem Res*, 2016, 49: 2424–2434
12 Zhu L, Zhong W, Qiu C, Lyu B, Zhou Z, Zhang M, Song J, Xu J, Wang J, Ali J, Feng W, Shi Z, Gu X, Ying L, Zhang Y, Liu F. *Adv Mater*, 2019, 31: 1902899
13 Zhao R, Lin B, Feng J, Dou C, Ding Z, Ma W, Liu J, Wang L. *Macromolecules*, 2019, 52: 7081–7088
14 Yao H, Bai F, Hu H, Arunagiri L, Zhang J, Chen Y, Yu H, Chen S, Liu T, Lai JYL, Zou Y, Ade H, Yan H. *ACS Energy Lett*, 2019, 4: 417–422
15 Zhou N, Dudnik AS, Li TING, Manley EF, Aldrich TJ, Guo P, Liao HC, Chen Z, Chen LX, Chang RPH, Facchetti A, Olvera de la Cruz M, Marks TJ. *J Am Chem Soc*, 2016, 138: 1240–1251
16 Jung J, Lee W, Lee C, Ahn H, Kim BJ. *Adv Energy Mater*, 2016, 6: 1600504
17 Chen D, Yao J, Chen L, Yin J, Lv R, Huang B, Liu S, Zhang ZG, Yang C, Chen Y, Li Y. *Angew Chem Int Ed*, 2018, 57: 4580–4584
18 Kolhe NB, Lee H, Kuzuhara D, Yoshimoto N, Koganezawa T, Jenekhe SA. *Chem Mater*, 2018, 30: 6540–6548
19 You H, Kim D, Cho HH, Lee C, Chong S, Ahn NY, Seo M, Kim J, Kim FS, Kim BJ. *Adv Funct Mater*, 2018, 28: 1803613
20 Yang J, Xiao B, Tajima K, Nakano M, Takimiya K, Tang A, Zhou E. *Macromolecules*, 2017, 50: 3179–3185
21 Liu M, Yang J, Yin Y, Zhang Y, Zhou E, Guo F, Zhao L. *J Mater Chem A*, 2018, 6: 414–422
22 Yang J, Yin Y, Chen F, Zhang Y, Xiao B, Zhao L, Zhou E. *ACS Appl Mater Interfaces*, 2018, 10: 23263–23269
23 Li Y, Meng H, Liu T, Xiao Y, Tang Z, Pang B, Li Y, Xiang Y, Zhang G, Lu X, Yu G, Yan H, Zhan C, Huang J, Yao J. *Adv Mater*, 2019, 31: 1904585
24 Shi S, Chen P, Chen Y, Feng K, Liu B, Chen J, Liao Q, Tu B, Luo J, Su M, Guo H, Kim MG, Facchetti A, Guo X. *Adv Mater*, 2019, 31: 1905161
25 Meng Y, Wu J, Guo X, Su W, Zhu L, Fang J, Zhang ZG, Liu F, Zhang M, Russell TP, Li Y. *Sci China Chem*, 2019, 62: 845–850
26 Zhang ZG, Yang Y, Yao J, Xue L, Chen S, Li X, Morrison W, Yang C, Li Y. *Angew Chem Int Ed*, 2017, 56: 13503–13507
27 Hwang YJ, Earmme T, Courtright BAE, Eberle FN, Jenekhe SA. *J Am Chem Soc*, 2015, 137: 4424–4434
28 Wu J, Meng Y, Guo X, Zhu L, Liu F, Zhang M. *J Mater Chem A*, 2019, 7: 16190–16196
29 Li Z, Ying L, Zhu P, Zhong W, Li N, Liu F, Huang F, Cao Y. *Energy Environ Sci*, 2018, 12: 157–163
30 Kim SW, Wang Y, You H, Lee W, Michinobu T, Kim BJ. *ACS Appl Mater Interfaces*, 2019, 11: 35896–35903
31 Zhang M, Guo X, Ma W, Ade H, Hou J. *Adv Mater*, 2015, 27: 4655–4660
32 Yuan J, Zhang Y, Zhou L, Zhang C, Lau TK, Zhang G, Lu X, Yip HL, So SK, Beaupré S, Mainville M, Johnson PA, Leclerc M, Chen H, Peng H, Li Y, Zou Y. *Adv Mater*, 2019, 31: 1807577
33 Yuan J, Huang T, Cheng P, Zou Y, Zhang H, Yang JL, Chang SY, Zhang Z, Huang W, Wang R, Meng D, Gao F, Yang Y. *Nat Commun*, 2019, 10: 570
34 Yu R, Yao H, Cui Y, Hong L, He C, Hou J. *Adv Mater*, 2019, 31: 1902302
35 Jiang K, Wei Q, Lai JYL, Peng Z, Kim HK, Yuan J, Ye L, Ade H, Zou Y, Yan H. *Joule*, 2019, 3: 3020–3033
36 Huo L, Liu T, Sun X, Cai Y, Heeger AJ, Sun Y. *Adv Mater*, 2015, 27: 2938–2944
37 Moore JR, Albert-Seifried S, Rao A, Massip S, Watts B, Morgan DJ, Friend RH, McNeill CR, Sirringhaus H. *Adv Energy Mater*, 2011, 1: 230–240
38 Fabiano S, Chen Z, Vahedi S, Facchetti A, Pignataro B, Loi MA. *J Mater Chem*, 2011, 21: 5891–5896
39 Eisner FD, Azzouzi M, Fei Z, Hou X, Anthopoulos TD, Dennis TJS, Heeney M, Nelson J. *J Am Chem Soc*, 2019, 141: 6362–6374
40 Zhang ZG, Qi B, Jin Z, Chi D, Qi Z, Li Y, Wang J. *Energy Environ Sci*, 2014, 7: 1966
41 Ye L, Jiao X, Zhao W, Zhang S, Yao H, Li S, Ade H, Hou J. *Chem Mater*, 2016, 28: 6178–6185
42 Sinha SK, Sirota EB, Garoff S, Stanley HB. *Phys Rev B*, 1988, 38: 2297–2311
43 Min J, Luponosov YN, Gasparini N, Richter M, Bakirov AV, Shcherbina MA, Chvalun SN, Grodd L, Grigorian S, Ameri T, Ponomarenko SA, Brabec CJ. *Adv Energy Mater*, 2015, 5: 1500386
44 Rau U. *Phys Rev B*, 2007, 76: 085303
45 Deibel C, Strobel T, Dyakonov V. *Adv Mater*, 2010, 22: 4097–4111
46 Sun R, Guo J, Wu Q, Zhang Z, Yang W, Guo J, Shi M, Zhang Y, Kahmann S, Ye L, Jiao X, Loi MA, Shen Q, Ade H, Tang W, Brabec CJ, Min J. *Energy Environ Sci*, 2019, 12: 3118–3132
47 Wang Y, Qian D, Cui Y, Zhang H, Hou J, Vandewal K, Kirchartz T, Gao F. *Adv Energy Mater*, 2018, 8: 1801352